Mineralogical Magazine (2020), **84**, 640–652
doi:10.1180/mgm.2020.72

CAMBRIDGE UNIVERSITY PRESS

Review

Kagomé networks of octahedrally coordinated metal atoms in minerals: Relating different mineral structures through octahedral tilting

Ian E. Grey*

CSIRO Mineral Resources, Private Bag 10, Clayton South, Victoria 3168, Australia

Abstract

Kagomé nets of corner-connected triangles of atoms occur in diverse minerals, from the {111} anion arrays in perovskite-group minerals to natural metallic alloys like auricupride, $AuCu_3$, to the cation layers in atacamite-group minerals. We review here two- and three-dimensional kagomé networks in minerals where the kagomé node atoms are octahedrally coordinated in hexagonal tungsten bronze (HTB) arrays. Octahedral tilting, coupled with capping of the apical anions of the triangular groupings of octahedra in the HTB layers, gives rise to several important mineral groups, including pyrochlores, alunite-supergroup minerals, zirconolite and weberite polytypes and spinel-group minerals, as a function of the magnitude and type of the octahedral tilting.

Keywords: kagomé nets, hexagonal tungsten bronze arrays, octahedral tilting, pyrochlore, weberite, zirconolite, alunite-group minerals, unit-cell intergrowth minerals

(Received 14 August 2020; accepted 15 September 2020; Accepted Manuscript published online: 17 September 2020; Associate Editor: G. Diego Gatta)

Introduction

The kagomé net of corner-connected triangles is a common structural component of many different minerals. It been the subject of intensive study in recent years because of its unusual magnetic properties including magnetic frustration, as typified by Fe^{3+} jarosite-group minerals (Pati and Rao, 2008). The kagomé net was first named by the Japanese physicist Itiro Syôzi (1951), based on its resemblance to the woven patterns of bamboo baskets, where the interlacing laths form triangular and hexagonal holes. The net is well represented in art and architecture as trihexagonal tiling, one of the semi-regular tilings by regular polygons (Fig. 1a). It is a combination of triangular and hexagonal tiling such that around each vertex, two hexagons and two triangles alternate, giving the Schläfli symbol 6.3.6.3 (O'Keeffe and Hyde, 1980). The tiling and its central six-pointed star (hexagram) have been used as decorative motifs since antiquity. When metal atoms at the nodes of the net have octahedral coordination with corner sharing connectivity between the octahedra it is referred to as a kagomé network (Pati and Rao, 2008). The anion arrangement was first described in the tungsten bronze $Rb_{0.27}WO_3$ (Magneli, 1952) and has become known as hexagonal tungsten bronze (HTB). This net, with symbol 3.4.6.4 is another semi-regular tiling found in ornament (Fig. 1b).

Kagomé nets are ubiquitous in mineral structures. In perovskite-group minerals and ReO_3-related minerals like bernalite, $Fe(OH)_3$ (Birch *et al.*, 1992), the {111} planes of anions form kagomé nets, while natural metallic alloys like auricupride, $AuCu_3$, and the sulfate mineral sulphohalite, $Na_6FCl(SO_4)_2$ have the antiperovskite structure with {111} kagomé nets of metal atoms (Krivovichev, 2008). In the atacamite family of minerals, typified by herbertsmithite, $Cu_3Zn(OH)_6Cl_2$, the Cu^{2+} cations occupy the nodes of a three dimensional (3D) kagomé network of edge-shared $Cu(OH,Cl)_6$ octahedra. This family of minerals has been studied in detail as candidates for quantum spin liquids (Malcherek *et al.*, 2018). Spinel-group and pyrochlore-group minerals also have 3D kagomé networks, with the nodes forming a corner-connected tetrahedral framework, while alunite-supergroup minerals have two-dimensional kagomé networks. Minerals containing ordered intergrowths of kagomé networks are also known. They include phyllotungstite and pittongite, with intergrowths of HTB and pyrochlore layers (Grey *et al.*, 2006) and perhamite-group minerals with intergrowth of HTB and zeolite (Mills *et al.*, 2012). We present here a consideration of kagomé HTB networks in minerals from the perspective of tilting of the octahedra.

The HTB structure

The HTB compounds have the general formula A_yBX_3, $y \leq \frac{1}{3}$, where A is a large univalent cation such as K, Rb and Cs; B is most commonly W (W^{6+}/W^{5+}) or Fe (Fe^{3+}/Fe^{2+}); and X is O or F. The aristotype HTB structure has space group *P6/mmm* with the atoms located at the following Wyckoff sites (italics are used for atom sites and non-italics for atoms in the chemical formulae): *A* site = 1*b* (0,0,½); *B* = 3*f* (½,0,0); *X*a = 3*g* (½,0,½); and *X*e = 6*l* (*x*,2*x*,0) with $x = 1/(3+\sqrt{3}) = 0.211$ (Whittle *et al.*, 2015). Xa and Xe are apical and equatorial anions.

*Author for correspondence: Ian E. Grey, Email: Ian.Grey@csiro.au
Cite this article: Grey I.E. (2020) Kagomé networks of octahedrally coordinated metal atoms in minerals: Relating different mineral structures through octahedral tilting. *Mineralogical Magazine* **84**, 640–652. https://doi.org/10.1180/mgm.2020.72

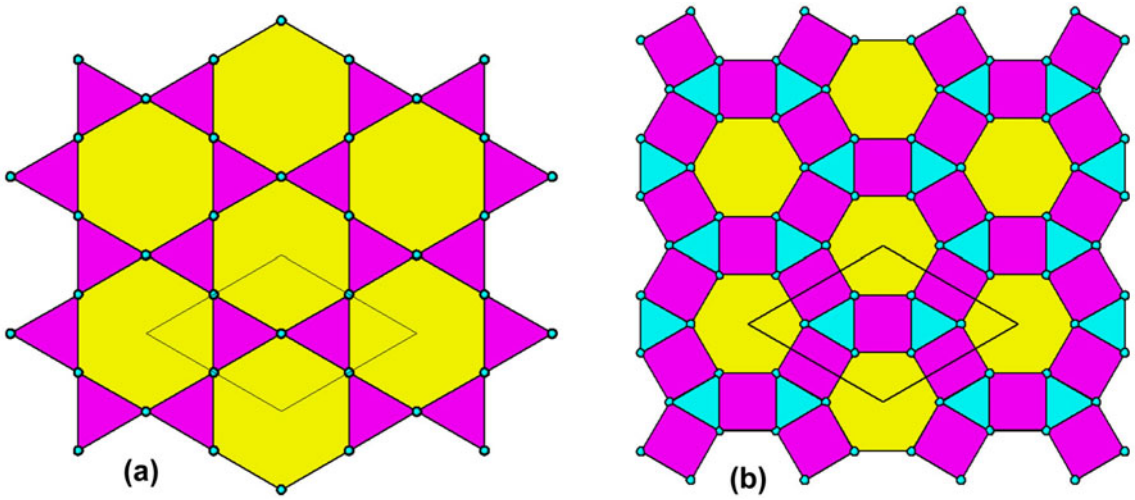

Fig. 1. (*a*) Trihexagonal tiling. Nodes (blue circles) correspond to a kagomé net. (*b*) Tiling in which the nodes correspond to the equatorial anions of a hexagonal tungsten bronze network of corner-connected octahedra, centred by kagomé net cations.

The kagomé net of B cations has octahedral coordination by X anions and the octahedra share corners to form triangular groupings of octahedra around large hexagonal cavities as shown in Fig. 2a. Normal to the plane of the Figure the layers of octahedra share corners. The cell parameters are related to the octahedral bond length d by the following expressions: $a = \sqrt{2(1+\sqrt{3})}d$ and $c = 2d$. Using the Gagné and Hawthorne (2015) bond-valence parameters for undistorted $W^{6+}O_6$ octahedra, d is 1.909 Å, giving $a = 7.376$ Å and $c = 3.818$ Å in WO_3. In M_xWO_3, a portion of the W is pentavalent and the parameters will be larger. e.g. for $x = ⅓$, the cell parameters based on undistorted octahedra are $a = 7.426$ Å and $c = 3.844$ Å.

The HTB structure was first solved by Magneli (1953), for $Rb_{0.27}WO_3$ in space group $P6_3/mcm$ with cell parameters $a =$ 7.39 Å and c = 7.54 Å. The doubled c axis is due to small displacements of the W atoms which reverse their direction from one layer to the next (second-order Jahn–Teller effect for the d^0 W^{6+} cation, Kunz and Brown, 1995). No ordered tilting of the octahedra is possible in $P6_3/mcm$ as it would be inconsistent with the c glide. Pye and Dickens (1979) conducted a structural study on $K_{0.26}WO_3$, using neutron diffraction which is more sensitive to the oxygen atoms and observed reflections, $h0l$, $l = 2n + 1$ that violate the c glide. They refined the structure in $P6_322$ and found that the planes of oxygen atoms that are coplanar with W in $P6_3/mcm$ are 'puckered' in $P6_322$. As described by Whittle *et al.* (2015) this puckering corresponds to ordered octahedral tilting about 2-fold axes as shown in Fig. 2b. This tilting scheme is a type of 'breathing' movement of the octahedra, whereby the apical anions, Xa, of triangular groups of corner-linked octahedra move inwards and the apices of the surrounding triangular groups move outwards. The HTB aristotype structure combined with this tilt system has space group $P6_3/mmc$, but it is lowered to $P6_322$ when the W displacements are included.

For the octahedral connectivity to be maintained as the octahedra are tilted there has to be a shrinkage in the unit-cell dimensions. The decrease in the cell parameters as a function of tilt angle, Φ, for the HTB $P6_3/mmc$ structure, with doubled c axis relative to the aristotype, is $a = \sqrt{2(1+\sqrt{3}\cos\Phi)}d$, $c = 4d\cos\Phi$. For HTB structures previously refined in $P6_3/mcm$ (Magneli, 1953; Labbé, 1978) the reported unit-cell parameters are generally smaller than calculated for the aristotype structure and these equations can be used to estimate the tilting angle. For A_xWO_3, A = K, Rb and Cs, tilting angles of the order of 5° are calculated. For the compound $Cs_{0.29}WO_3$, Prinz *et al.* (1992) conducted a single-crystal X-ray diffraction (XRD) refinement in $P6_322$ and noted that the displacement of O2 (≡ Xa) corresponds to a tilting angle of 6.7(4)° whereas the displacement of O1(≡ Xe) corresponds to a tilt angle of 4.6(8)°, indicating that the octahedra do not tilt as perfectly rigid bodies.

Campbell *et al.* (2018) applied group theoretical analysis to determine all possible octahedral tilting modes for HTB structures, with the octahedra considered as rigid units. They found ten subgroups of the aristotype $P6/mmm$ structure where tilting maintained the integrity of the octahedral corner linkages for very small tilt angles. Whittle *et al.* (2018) noted that only three of the subgroups have each of the octahedra tilting through the same angle and are most likely to occur. These have space groups $P6_3/mmc$ (Fig. 2b), $Cmcm$ (with $b = \sqrt{3}a$) and $P6/mmm$ with doubled a, b and c parameters. Whittle *et al.* (2015) noted that there have been no reports in the literature of structures with the third tilt system.

Examples of compounds with $Cmcm$-type tilting are the fluorides, β-BF_3, B = Al and Ga (Le Bail *et al.*, 1988) and $(H_2O)_{0.33}FeF_3$ (LeBlanc *et al.*, 1983). The tilting scheme in these compounds is shown in Fig. 2c. It involves different combinations of 2-fold rotation axes to that shown in Fig. 2b. The octahedral tilting results in the equilateral triangles of apical anions in adjacent triangular groupings of octahedra in the aristotype being converted to pairs of compressed and elongated isosceles triangles. The mean tilt angle increases from 7.2° in β-AlF_3 to 12.9° in β-GaF_3 to 14.5° in $(H_2O)_{0.33}FeF_3$. The increase in tilt angle follows the order of increasing electronegativity of B, with Al < Ga < Fe. This is consistent with the octahedral tilting being driven by B ns–X $2p$ σ-bonding covalency in these HTB compounds, as proposed for the A-cation-absent perovskite TeO_3 by Mizoguchi *et al.* (2004). In the HTB structures the triangular groupings of octahedra (Fig. 2a) have strongly bent B–X–B linkages (~150°) that are more conducive to covalent σ-bonding than the 180° B–X–B linkages in perovskite. The HTB oxides, $ANbW_2O_9$, A = K and Rb, also have the octahedral tilt system shown in Fig. 2c, with a lowering of space group symmetry to $Cmc2_1$ to take

https://doi.org/10.1180/mgm.2020.72 Published online by Cambridge University Press

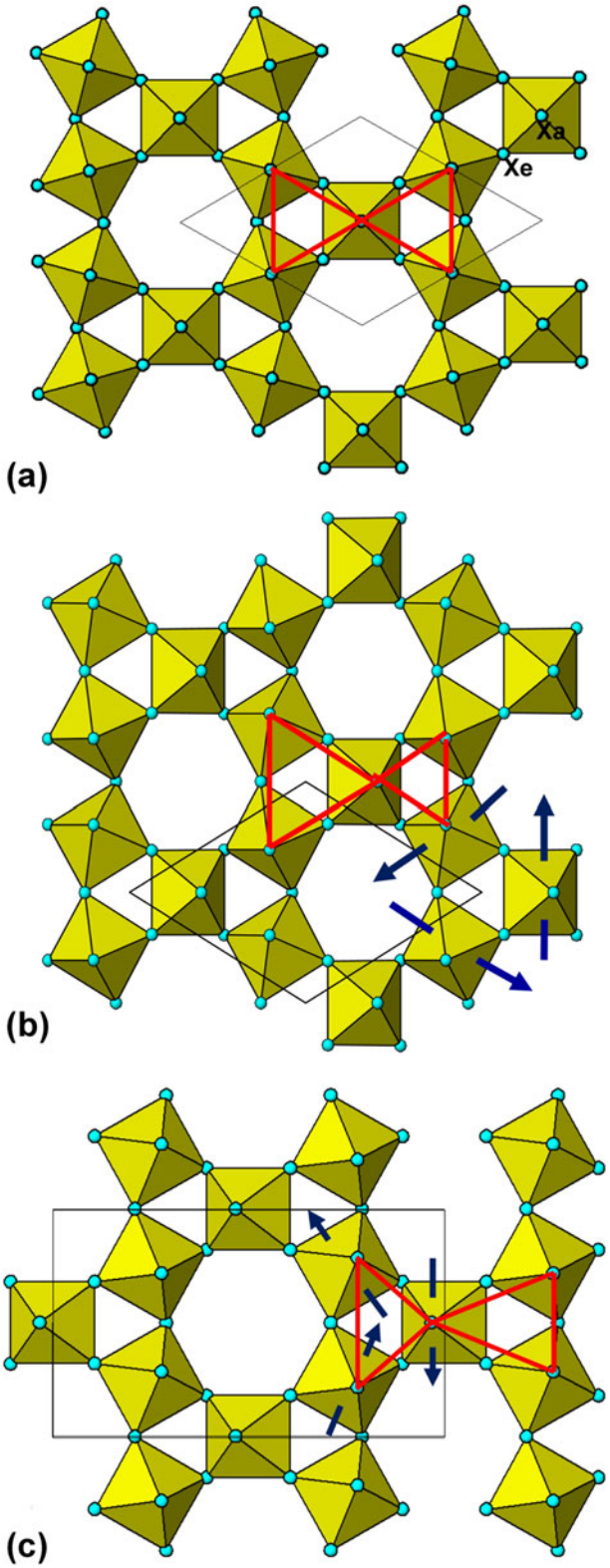

Fig. 2. (*a*) HTB layer of corner-connected octahedra. (*b*) P6$_3$/*mmc*-type tilting of octahedra. (*c*) *Cmcm*-type tilting of octahedra.

account of polar displacements of the *B*-site cations (McNulty *et al.*, 2019).

Thus far, we have considered only HTB structures in which the HTB layers are corner-connected along [001] to form 3D

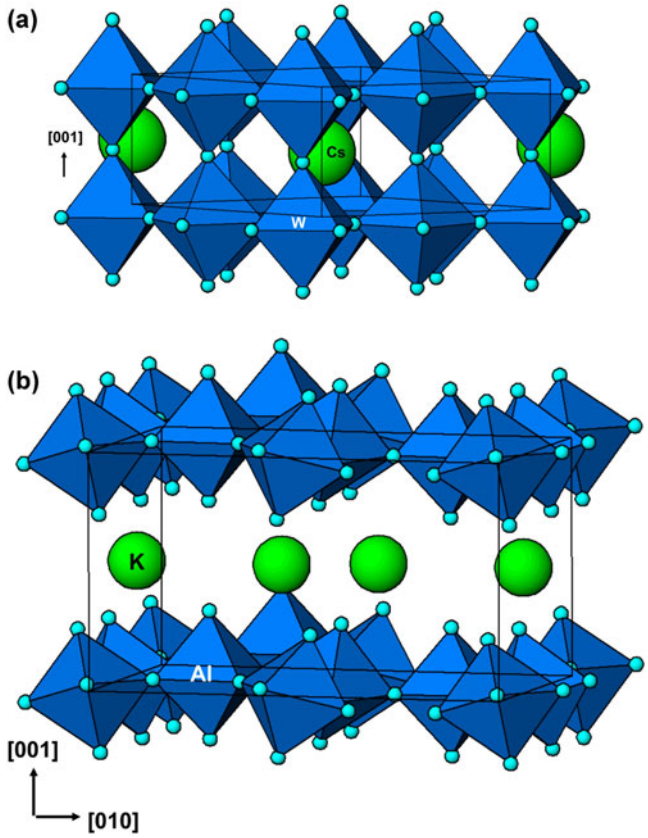

Fig. 3. (*a*) Corner-connection of HTB layers in Cs_xWO_3. (*b*) Separate HTB layers in $K_3Al_3F_{12}.H_2O$.

frameworks as shown in Fig. 3a. Le Bail and co-workers (Le Bail *et al.*, 1988; Le Bail *et al.*, 1990; Le Bail, 2009; Courbion *et al.*, 1976) have characterised the structures of a number of hydrous alkali aluminium fluorides which have in common a separation of the HTB layers with alkali cations and water molecules between the layers, so that the composition of the layer is $B(Xe)_{4/2}(Xa)_2 = BX_4$. The example of $K_3Al_3F_{12}{\cdot}H_2O$ (Le Bail 2009) is shown in Fig. 3b. Inspection of the structure reported by Le Bail (2009) shows that the octahedral tilt system is the *Immm* system of Campbell *et al.* (2018) in which one third of the octahedra are untilted.

Despite the great variety of synthetic HTB structures with various octahedral tilt systems, there have been only a few natural examples reported. Only one mineral with corner-connected HTB layers as in Fig. 3a has been published. It is wumuite, $KAl_{0.33}W_{2.67}O_9$, with space group *P6/mmm* and unit-cell parameters $a = 7.2952(5)$ and $c = 3.7711(3)$ Å (Li and Xue, 2018). A second mineral, tewite, $K_{1.5}(Te_{1.25}W_{0.25})W_5O_{19}$, with space group *Pban* and unit-cell parameters $a = 7.2585((4)$, $b = 25.810(1)$ and $c = 3.8177(2)$ Å has a modified HTB structure (Li *et al.*, 2019). In tewite, 10 Å wide slabs of HTB parallel to (010) are interconnected via corner sharing with strongly distorted TeO_6 octahedra. The octahedra in the HTB slabs are not tilted. The mineral meymacite, $WO_3.nH_2O$, is usually reported as being amorphous but a recent transmission electron microscopy and Raman microscopy study of iron-bearing meymacite by Tarassov and Tarassova (2018) showed that it comprises nano-scale domains with the same kind of HTB derivative structure as in the synthetic phase $WO_3{\cdot}\frac{1}{3}H_2O$ (Gerand *et al.*, 1981). In this structure, with space group *Fmm*2 and

https://doi.org/10.1180/mgm.2020.72 Published online by Cambridge University Press

cell parameters $a = 7.359(3)$, $b = 12.513(6)$ and $c = 7.704(5)$ Å, successive HTB layers along [001] are shifted by $a/2$, so that only two-thirds of the octahedra in adjacent layers are corner-connected. The other one third of octahedra have their apices (O═W–H_2O) above and below the hexagonal rings in adjacent layers.

In contrast to the limited number of natural HTB compounds with corner-connected layer structures, there are several extended families of minerals for which the structures are built from HTB layers where the apical anions are not shared between layers as in Fig. 3a but are capped by polyhedra. The type and size of the capping polyhedron is linked to the magnitude of octahedral tilting as will be described in the following sections.

Capped HTB structures

As shown in Fig. 2b, the $P6_3/mmc$-scheme of tilting of the HTB octahedra alternately expands and contracts the equilateral triangles of apical anions. The shortening of the distance between the anions in the smaller triangle as a function of the tilting angle is given by the equation below for undistorted octahedra.

$$\mathrm{Xa{-}Xa} = e/2[1 + \sqrt{3}\cos\Phi - \sqrt{6}\sin\Phi] \quad (1)$$

Where e is the octahedral edge distance. With no tilting the Xa–Xa separation is $e/2(1+\sqrt{3}) = 0.5a_{hex}$, which is of the order of 3.72 Å for HTB compounds discussed above. We consider different cases of octahedral tilting so that the Xa–Xa distance decreases to match the polyhedral edge-distance of various polyhedra, leading to different HTB derivative structures.

Pyrochlore minerals and HTB-pyrochlore intgergrowths

Pyrochlore was the name originally given to a mineral of composition $(Na,Ca)_2Nb_2O_6(OH,F)$, but is now the name of a mineral group with general composition (for stoichiometric minerals) $A_2B_2X_6Y$ (Atencio *et al.*, 2010). The aristotype has cubic symmetry, $Fd\bar{3}m$, with $a \approx 10.4$ Å and atoms at the Wyckoff sites: A site = 16*d* (½,½,½); B = 16*c* (0,0,0); X = 48*f* (x,⅛,⅛); Y = 8b (⅜,⅜,⅜) where $x = 0.3125$ for undistorted BX_6 octahedra and $x = 0.375$ for undistorted AX_6Y_2 cubes (Subramanian *et al.*, 1983). The much stronger bonding of the B cations to X forces the value of x to be close to 0.3125, leading to strong distortion of the A cation-centred polyhedra. This is an inherent source of strain in pyrochlore structures.

The pyrochlore structure is usually described as an anion-deficient fluorite derivative structure with face-centred cubic (*fcc*) stacking of alternating A_3B and B_3A metal atom layers parallel to the $\{111\}_{\mathrm{fluorite}}$ planes (Subramanian *et al.*, 1983; Fuentes *et al.*, 2018; Trump *et al.*, 2018). Both the A and B atoms form 3D kagomé arrays of anion-centred corner-connected tetrahedra, YA_4 and $\square B_4$ ($\square$ = vacancy) (Pannetier and Lucas, 1970) as shown in Fig. 4. The composition of the net of YA_4 tetrahedra is A_2Y and that of the $\square B_4$ net with octahedral coordination of the B atoms by X is B_2X_6, leading to a representation of the pyrochlore formula that emphasises the independence of the two sublattices, $B_2X_6.A_2Y$. Defect pyrochlore minerals have vacancies at the A and Y sites and incorporation of H_2O giving $A_{2-m}B_2X_6Y_{1-n}{\cdot}pH_2O$ (Hogarth, 1977) although minor loss of X can also occur under extreme alteration (Lumpkin and Ewing 1995).

The pyrochlore B_2X_6 framework can be derived formally from BX_4 HTB layers by increasing the octahedral tilt angle until Xa–Xa decreases to match the BX_6 octahedral edge distance. With Xa–Xa = e, equation 1 is used to calculate the tilt angle, giving 15.8° for undistorted octahedra. At this tilt angle the same type of BX_6 octahedron that forms the HTB layer can exactly cap the smaller triangles of apical anions, Xa, as shown in Fig. 5. Adding successive HTB layers with capping of the smaller triangles on both sides of the layers leads directly to the B_2X_6 octahedral framework in pyrochlore. Formally it is given by $3BX_4 + B(\mathrm{cap}) = B_4X_{12}$ (no reaction mechanism implied).

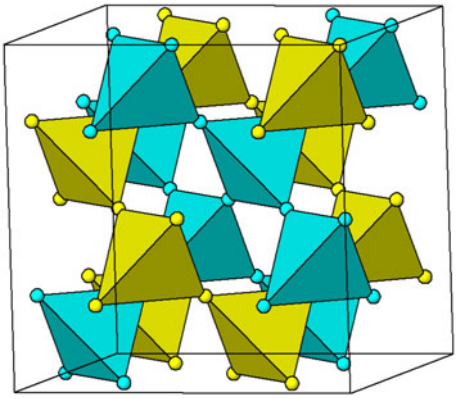

Fig. 4. Corner connected A_4 tetrahedra (blue) and B_4 tetrahedra (yellow) in pyrochlore

Since the establishment of a nomenclature scheme for the pyrochlore supergroup of minerals (Atencio *et al.*, 2010; Christy and Atencio, 2013) there have been numerous publications on new minerals of the supergroup with high quality single-crystal refinements of the structures. We have calculated the octahedral tilt angles from the published structural data, after first converting the cubic $Fd\bar{3}m$ cells and coordinates to $R\bar{3}m$ hexagonal cells for ease of calculation of the tilt angles. In the hexagonal cell the tilt angle can be calculated separately from the vertical displacement of the equatorial anions, Xe, and from the horizontal displacement of the apical anions, Xa. The results are given in Table 1. The minerals hydrokenoralstonite with Al in the B site (Atencio *et al.*, 2017) and hydrokenoelsmoreite-3*C* with W^{6+} in the B site, (Mills *et al.*, 2016) both have measured tilt angles that agree with the value of 15.8° calculated from equation 1.

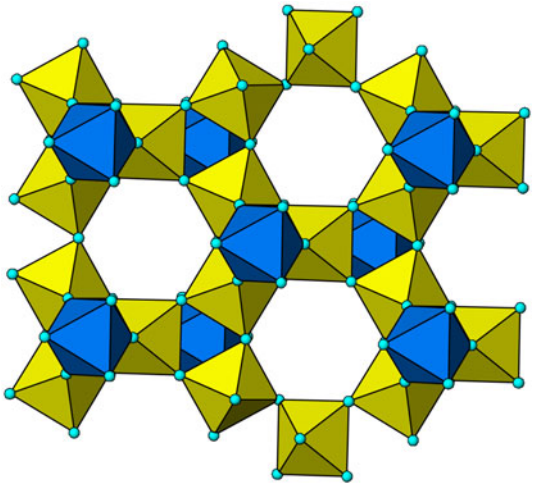

Fig. 5. Capping of small triangles of Xa anions by octahedra in pyrochlore {111} HTB layer.

https://doi.org/10.1180/mgm.2020.72 Published online by Cambridge University Press

Table 1. Structural data for pyrochlore-group minerals and compounds.

Mineral	Formula	Cell (Å)	*x* coord. for O1	Φ calc. (°)	Φ, from Xe, Xa, av. (°)	B–X–B (°)	Ref.
Cubic pyrochlores							
Defect pyrochlore	$\square_2TaW(O,OH)_6$	10.444	0.3094(3)	15.8	15.1, 16.7 <15.9>	142.9	[1]
Hydrokenoralstonite	$(\square,Na)_2(Al,Mg)_2(F,OH)_6(H_2O)$	9.845	0.3127(1)	"	15.8, 15.8 <15.8>	141.0	[2]
Hydrokenoelsmoreite-3*C*	$(\square,Na,H_2O)_2(W,Fe)_2(O,OH)_6(H_2O)$	10.306	0.3128(3)	"	15.8, 15.8 <15.8>	141.1	[3]
Hydroxynatropyrochlore	$(Na,Ca,Ce)_2Nb_2O_6(OH)$	10.328	0.3185(6)	15.8	17.1, 14.0 <15.6>	137.6	[4]
Fluornatropyrochlore	$(Na,REE,Ca)_2Nb_2(O,OH)_6F$	10.505	0.3167(10)	"	16.7, 14.3 <15.5>	138.7	[5]
Fluorcalciopyrochlore	$(Ca,\square)_2Nb_2(O,OH)_6F$	10.420	0.3175(3)	"	16.9, 14.3 <15.6>	138.2	[6]
Fluornatromicrolite	$(Na,Ca,Bi)_2Ta_2O_6F$	10.445	0.3172(5)	15.8	16.9, 14.5 <15.7>	138.6	[7]
Hydrokenomicrolite	$(\square,Ba,Sr)_2Ta_2(O,OH)_6(H_2O)$	10.454	0.3191(14)	"	17.3, 13.9 <15.6>	137.3	[8]
Oxybismutomicrolite	$(Bi,Na,Ca)_2Ta_2O_6O$	10.475	0.3181(5)	"	17.1, 14.2 <15.6>	137.9	[9]
Oxyplumboroméite	$Pb_2Sb_2O_6O$	10.378	0.3228(5)	15.8	18.1, 12.9 <15.5>	135.2	[10]
Fluorcalcioroméite	$(Ca,Sb^{3+})_2(Sb^{5+},Ti)_2O_6F$	10.299	0.3233(2)	"	18.2, 12.8 <15.5>	134.9	[11]
Oxycalcioroméite	$Ca_2Sb_2O_6O$	10.304	0.3241(2)	"	18.5, 13.6 <16.0>	134.5	[12]
Fluornatroroméite	$(Na,Ca)_2Sb_2(O,OH)_6F$	10.265	0.3234(2)	"	18.2, 12.7 <15.5>	134.9	[13]
Rhombohedral pyrochlores							
Fluornatrocoulsellite	$CaNa_3AlMg_3F_{14}$	7.162		19.5	19.8, 16.5 <18.2>	140.8 Mg–F–Al	[14]
		17.597				131.6 Mg–F–Mg	
Synthetic	$MnLa_3MnSb_3O_{14}$	7.549		11.2	11.9, 9.0 <10.5>	126.6 Sb–O–Mn	[15]
		17.798				138.6 Sb–O–Sb	
Inverse pyrochlore	$\square_4NaAl_3F_{12}Cs_2$	7.026		3.5	4.5, 4.3 <4.4>	128.7 Al–F–Na	[16]
		18.244				147.6 Al–F–Al	

References: [1] Groult *et al.* (1982); [2] Atencio *et al.* (2017); [3] Mills *et al.* (2016); [4] Ivanyuk *et al.* (2019); [5] Yin *et al.* (2015); [6] Bonazzi *et al.* (2006); [7] Witzke *et al.* (2011); [8] Andrade *et al.* (2013); [9] Kasatkin *et al.* (2020); [10] Halenius and Bosi (2013); [11] Atencio *et al.* (2013); [12] Biagioni *et al.* (2013); [13] Matsubara *et al.* (1996); [14] Mumme *et al.* (2010); [15] Fu and Ijdo (2014); and [16] Courbion *et al.* (1976).

These two minerals have almost perfect octahedra with X–B–X angles of 90° and all X–X edges equal. The other minerals listed in Table 1 have tilt angles that deviate from the ideal value, with the deviation increasing from pyrochlore-group minerals (B = Nb) to microlites (B = Ta) to roméite-group minerals (B = Sb). For all these minerals the cubic cell *x* coordinate for the anion is higher than the ideal value of 0.3125 that corresponds to a perfect octahedron. With increasing *x* above this value the geometry is described as a flattened trigonal prism (Subramanian *et al.*, 1983). It is this distortion that results in different experimental tilt angles being calculated from the Xe and Xa anions, although the average stays close to the calculated value of 15.8° from equation 1.

As seen from Table 1, within each pyrochlore group the trigonal antiprism distortion does not appear to depend significantly on the A cation, with similar distortions for A cations varying from Pb^{2+} and Bi^{3+} to Ca^{2+}, Na^+ and H_2O (defect keno pyrochlores). There is however, a clear inverse correlation between the magnitude of the distortion and the B–X–B angle. The distortion is greatest for B = Sb which has the smallest B–X–B angles. Sb is the most electronegative of the B elements in Table 1, which suggests that the distortion occurs to increase the B *n*s–X 2*p* covalent σ-bonding strength, as we noted earlier for the HTB compounds.

The cubic pyrochlores in Table 1 all have a single B cation, so the tilt angle calculated from equation 1 is the same for all. In contrast, rhombohedral pyrochlores, with 1:3 ordering of the A and B cations, $AA'_3BB'_3X_{14}$, have widely different tilt angles, depending on the relative sizes of the B and B' cations. In fluornatrocoulsellite, $CaNa_3AlMg_3F_{14}$ (Mumme *et al.*, 2010) the HTB cation, Mg^{2+}, is considerably larger than the capping cation Al^{3+}, and so larger tilt angles are required for the triangles of apical anions of the HTB layer to fit to the base of the capping octahedra. With Xa–Xa and *e* in equation 1 calculated for undistorted AlF_6 and MgF_6 octahedra from bond-valence sum (BVS) parameters for fluorides (Brese and O'Keeffe, 1991) the calculated tilt angle is 19.5°. This compares with a mean value of 18.2° obtained from the refined crystal structure. The MgF_6 octahedra are relatively distorted with F–Mg–F angles in the range 84.1 to 91.4 and F–F edge distances of 2.63 to 2.91 Å. The tilted HTB layers in fluornatrocoulsellite are shown in Fig. 6a.

In contrast to fluornatrocoulsellite, the 1:3 ordered rhombohedral pyrochlore $Mn^{2+}La_3Mn^{2+}Sb_3O_{14}$ (Fu and Ijdo, 2014) has a smaller HTB cation, Sb^{5+}, than the capping cation, Mn^{2+}. In this case smaller octahedral tilts are required to match Xa–Xa to the base of the capping octahedron. For undistorted octahedra, application of equation 1 gives a tilt angle of 11.2°, compared to 10.5° measured from the refined structure. The MnO_6 polyhedron is a flattened trigonal antiprism with angles of 79.9 and 100.1°.

An extreme example of B cation size difference in 1:3 ordered rhombohedral pyrochlores is the defect pyrochlore of composition $\square_4NaAl_3F_{12}Cs_2$ (Courbion *et al.*, 1976). This is an example of the so-called inverse pyrochlores, where the very large Cs^+ cation occupies the 8*b* site normally occupied by the Y anion. The B cations in the HTB layers are Al^{3+} and the capping cations are Na^+. Application of equation 1 shows that a tilting angle of only 3.5° is required to match the capping NaF_6 to the HTB anions. The pyrochlore framework is shown in Fig. 6b. The Cs^+ cations have 15 anion neighbours with distances in the range 3.03 to 3.55 Å, giving a nearly ideal BVS of 1.10.

When the Cs is replaced by Rb or K the $P6_3/mmc$-type octahedral tilting system is unable to provide suitably sized cavities for the smaller cations. Instead, a different system of tilting occurs which involves puckering of the kagomé nets of Al^{3+} cations to meet the bonding requirements of K^+/Rb^+ (Le Bail *et al.*, 1990). The tilting system belongs to the *Immm* space-group type reported by Campbell *et al.* (2018). As shown in Fig. 7a the *Immm*-type tilting involves only two-thirds of the octahedra, which form [010] chains in $K_2NaAl_3F_{12}$; the other octahedra are untilted. The tilting changes the pairs of equilateral triangles of Xa anions to isosceles triangles. As a result of the tilting the untilted octahedra are displaced above and below the plane of

https://doi.org/10.1180/mgm.2020.72 Published online by Cambridge University Press

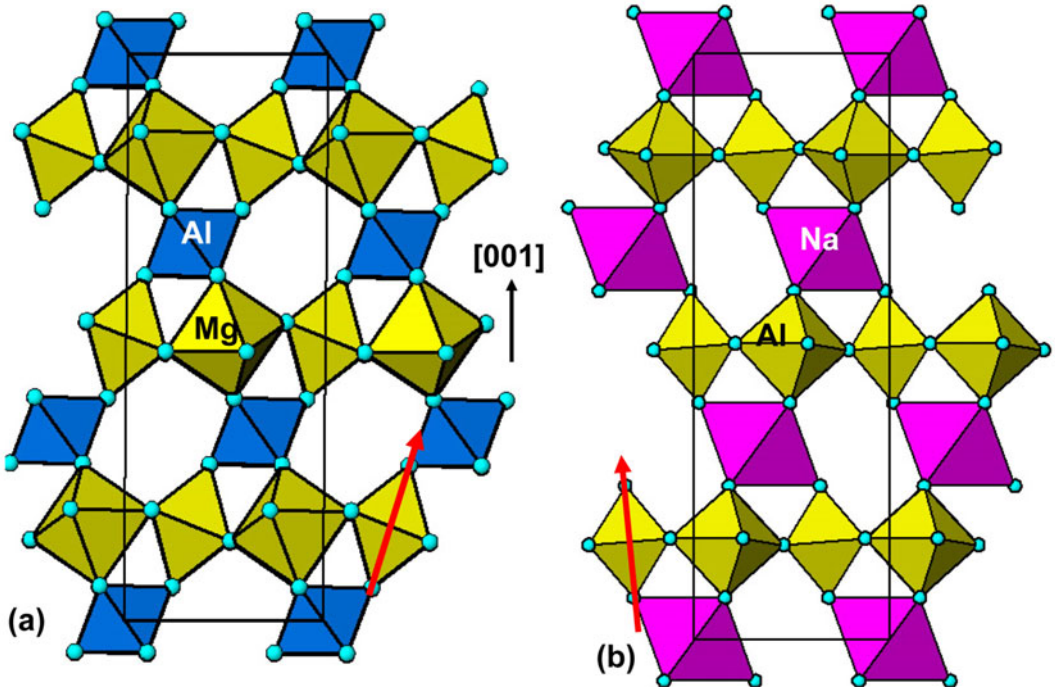

Fig. 6. [100] projections of the structures of rhombohedral pyrochlores (*a*) fluornatrocoulsellite, octahedral tilt angle = 19.5°; (*b*) $Cs_2NaAl_3F_{12}$, tilt angle = 3.5°. Tilts shown by red arrows.

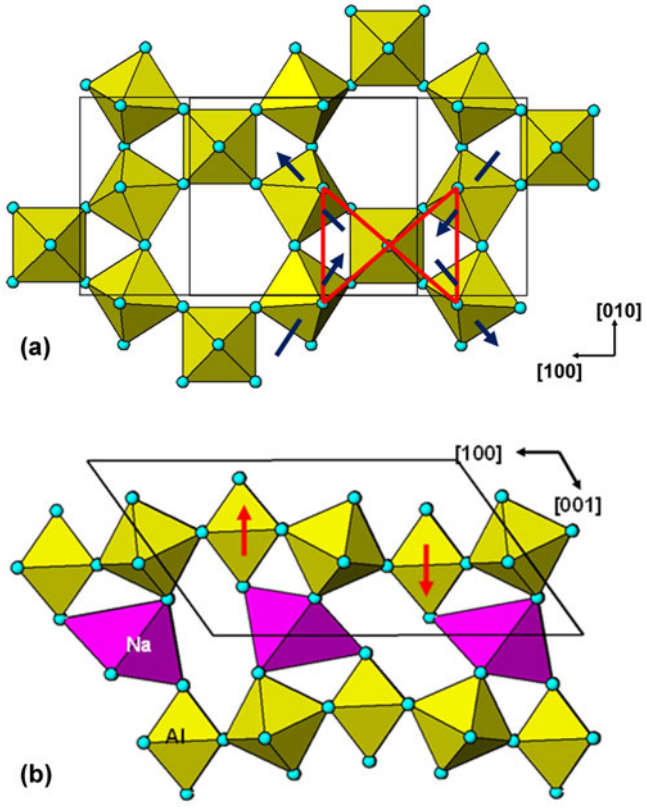

Fig. 7. (*a*) *Immm*-type tilting of octahedra in $K_2NaAl_3F_{12}$ as viewed along *c**. (b) [010] projection of $K_2NaAl_3F_{12}$ structure, showing large displacement of untilted octahedra along ***c**** (red arrows).

the tilted octahedra as shown in Fig. 7b. In $K_2NaAl_3F_{12}$ the displacements along ***c**** are ± 0.5 Å. The planar kagomé net of cations becomes strongly corrugated as a result. Such tilting cannot occur in corner-connected HTB structures without the breaking of interlayer corner connections, but in pyrochlore-type structures it can occur, albeit with strong distortion of the capping BX_6 polyhedra as shown in Fig. 7b for the NaF_6 polyhedron in $K_2NaAl_3F_{12}$..

The 1:3 ordered rhombohedral pyrochlores have quite different in-plane B–X–B and out-of-plane B'–X–B angles with the difference between them reversing when B' changes from being smaller than B to greater than B. For the antimony compound, the Sb–O–Sb angle of 138.6° is higher than the Sb–O–Sb angle in the four different roméite-group cubic pyrochlores in Table 1, which are in the narrow range 134.5 to 135.2°, suggesting that the bonding requirements for the A and A' cations are important in this case.

The crystal structure results for the mineral hydrokenoelsmoreite-3*C* (Mills *et al.*, 2016) require further consideration. In the refined structure the WO_6 octahedra are undistorted and the W is undisplaced from the ideal 16*c* site. This is in contrast to W in HTB compounds, A_xWO_3, where crystal structure studies show the W to be displaced from the centre of the octahedron by ~0.10 to 0.15 Å, consistent with a second-order Jahn Teller distortion for the d^0 cation (Pye and Dickens, 1979; Labbé *et al.*, 1978; Prinz, 1992). In addition W has a relatively high electronegativity, comparable with that for Sb according to the Pauling scale, and a similar B–X–B angle might be expected. A possible answer to this dilemma is that displacements of W and O do occur but they are short-range ordered and are manifested only indirectly by elevated atomic displacement parameters. The U_{eq} values are 0.023 $Å^2$ for W and 0.021 $Å^2$ for O in hydrokenoelsmoreite whereas they are much smaller at 0.007 $Å^2$ for Al

https://doi.org/10.1180/mgm.2020.72 Published online by Cambridge University Press

and 0.011 Å^2 for OH in the related defect pyrochlore hydrokenoralstonite (Atencio *et al.*, 2017). The U_{eq} values for hydrokenoelsmoreite correspond to root-mean-square displacements of ~0.15 Å. This is the same magnitude as the W displacements in HTB compounds and the anion displacements in the Sb pyrochlores.

The absence of long-range ordering of W displacements in hydrokenoelsmoreite is a specific example of the more general phenomenon of geometric frustration in the pyrochlore structure (McQueen *et al.*, 2008; Trump *et al.*, 2018). As shown in Fig. 4, the B cation kagomé network comprises a 3D array of corner-connected tetrahedra. Displacement of B involves 'breathing' or rotation of the B_4 tetrahedra and the inherent geometric frustration means that the displacements point in different directions, thus cancelling out in statistical displacements when modelled in $Fd\bar{3}m$. McQueen *et al.* (2008) compared neutron powder XRD refinements of $CaYNb_2O_7$ and other pyrochlores in space group $Fd\bar{3}m$, with and without displacement of Nb along <111>. Without displacement the isotropic displacement parameter for Nb in $CaYNb_2O_7$ was 0.019(1) Å^2. Refinement of the Nb (*x,x,x*) coordinate resulted in a displacement of 0.145 Å from the ideal position with a lowering of U_{eq} to 0.013(1) Å^2 and an improved fit to the data. A consequence of the distortion of the Nb kagomé network is that the Nb–O–Nb angle is changed from 132.4° in the ideal $Fd\bar{3}m$ structure to values of 125, 132.4 and 139.2° in the displaced-Nb structure. Similar results could be expected from local displacements of the B cations in hydrokenoelsmoreite and other minerals.

Given that the pyrochlore structure can be derived from the HTB structure by capping of the apical anions, the possibility exists for intergrowth of the two structure types. In nature this is confirmed for the minerals phyllotungstite (Walenta, 1984; Grey *et al.*, 2013) and pittongite (Birch *et al.*, 2007; Grey *et al.*, 2006). Phyllotungstite, $(\square,Pb,Cs)_{10}(W,Fe)_{14}(O,OH)_{42}(H_2O)_4$ is orthorhombic (pseudohexagonal), *Cmcm* with $a = 7.298$, $b = 12.640$ ($= \sqrt{3}a$) and $c = 19.582$ Å. The structure is shown in projection along [110] in Fig. 8. It comprises 6 Å wide blocks of pyrochlore intergrown along [001] with two HTB layers of width 3.8 Å, giving a *c* axis periodicity of $2 \times (6 + 3.8) = 19.6$ Å. An alternative description is in terms of ordered unit-cell twinning of the pyrochlore structure, where the twin planes lie between two HTB layers. The tilting of the octahedra in the HTB layers is required to match that of the octahedra in the pyrochlore blocks, and so ideally it has a magnitude of 15.8° (from equation 1). This is higher than for any reported HTB structures.

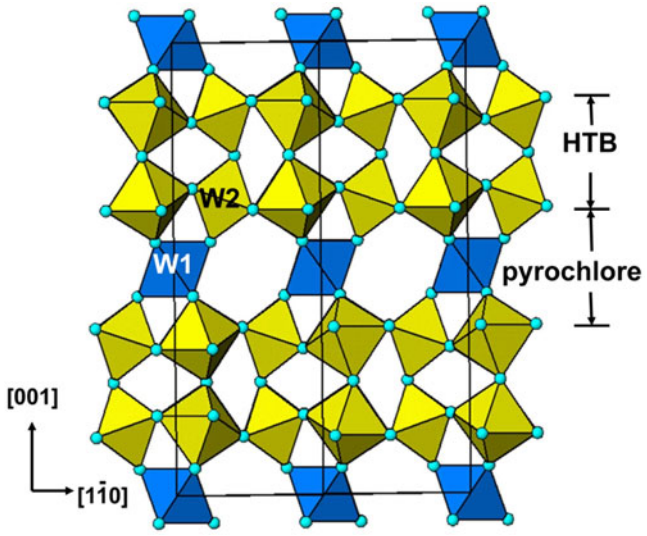

Fig. 8. [110] projection of the phyllotungstite structure.

In pittongite, $(\square,Na,H_2O)_{32}(W,Fe)_{36}(O,OH)_{108}(H_2O)_{12}$ there are both 6 Å and 12 Å wide pyrochlore blocks intergrown with double HTB layers, giving a *c* axis periodicity of $2\times (6 + 3.8 + 12 + 3.8) = 51.2$ Å (actual $c = 50.49$ Å). Again, the structure can be described as unit-cell twinning of pyrochlore blocks. In this case the pyochlore blocks are of two different widths. At the twin planes, pairs of HTB layers are corner-connected. In the system Bi_2O_3–Fe_2O_3–Nb_2O_5, synthetic intergrowth phases have been structurally characterised that correspond to 12 Å-wide pyrochlore block intergrown with HTB ($c = 2 \times (12 + 3.9) = 31.8$ Å) and to a rhombohedral form of the pittongite sequence with $c = 3 \times (6 + 3.9 + 12 + 3.9) = 77.4$ Å, demonstrating that long-range ordering of quite complex intergrowth sequences of the two structure types is possible (Grey *et al.*, 2007).

An intriguing example of a pyrochlore intergrowth structure has been reported by Crosnier *et al.* (1991) for the compound $Cs_8Nb_{10}O_{23}(Si_3O_9)_2$, with space group $P6_3/mmc$, $a = 7.342$ Å and $c = 22.166$ Å. In this compound HTB layers of corner-connected NbO_6 octahedra are capped on both sides by NbO_6, giving pyrochlore blocks of composition Nb_5O_{18}. The pyrochlore blocks are interconnected along [001] via corner sharing of the capping octahedra with cyclic Si_3O_9 clusters. Crosnier *et al.* (1991) describe the structure as an intergrowth of pyrochlore-type and benitoite-type ($BaTiSi_3O_9$)-type structures. The capping octahedra are common to both the benitoite blocks (with Nb replacing Ti) and the pyrochlore blocks. The intergrowth framework is then $[Nb_3O_{12}Nb_{2/2}O_{6/2}] + [Nb_{2/2}Si_3O_3O_{6/2}]$, where 2/2 and 6/2 indicate sharing between the two blocks. The Cs^+ cations occupy large cavities located between the hexagonal rings of the HTB layers and the Si_3O_9 rings.

Zirconolite minerals

Zirconolite was the name given to a monoclinic mineral of composition $CaZrTi_2O_7$, and it is now the group name for three different mineral polytypes with the same ideal formula and with substitutions of mainly rare earth elements (*REE*) for Ca and Nb, and Ta and Fe for Ti (Bayliss *et al.*, 1989). Like pyrochlore, the zirconolite structure can be described as an ordered anion-deficient fluorite derivative structure, with a *fcc* array of cations. However, while pyrochlore has an alternation of <111> fluorite cation layers of composition AB_3 and B_3A, the alternating layers of small and large cations in zirconolite have the compositions B_3B' and $A_2A'_2$. Ti^{4+} cations occupy both the kagomé net sites (B) and sites in the hexagonal rings within the net (B', displaced from the centre of the ring). The large cation layers contain parallel chains of edge-shared distorted cubes (A) and mono-capped trigonal antiprisms (A').

In the aristotype mineral, zirconolite-2*M*, with space group *C*2/*c* and cell parameters $a \approx 12.4$ Å, $b \approx 7.3$ Å, $c \approx 11.4$ Å and $\beta \approx 100.5°$ (Gatehouse *et al.*, 1981) the chains of large cations are oriented parallel to [110] and [1$\bar{1}$0] in successive $A_2A'_2$ layers. Zirconolite-3*T*, with trigonal space group $P3_121$ and cell parameters $a \approx 7.3$ Å and $c \approx 17.0$ Å (Grey *et al.*, 2003; Zubkova *et al.*, 2018), has the chains of large cations oriented parallel to [100], [010] and [110] in successive layers, so making angles of 120° with each other. Orthorhombic zirconolite-3*O*, with space group *Cmca*, $a \approx 7.3$ Å, $b \approx 14.1$ Å and $c \approx 10.2$ Å, differs

https://doi.org/10.1180/mgm.2020.72 Published online by Cambridge University Press

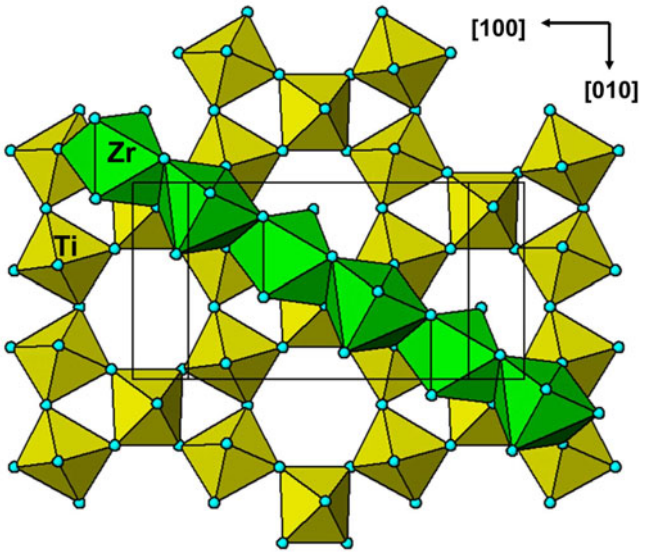

Fig. 9. Capping of HTB layer with ZrO_7 in zirconolite-2*M*. Alternate ZrO_7 polyhedra have their capping triangular faces pointing to the HTB layer below and the HTB layer above (not shown).

significantly from the other polytypes in that the kagomé net of small cations is not planar, but has a sawtooth shape with large (>1 Å) displacements of the cations out of the plane of the net (Chukanov *et al.*, 2019). The corner-connected octahedra do not have the HTB layer topology of *trans*-corner connection. There is periodic shearing along an octahedral edge so that there is a mixture of *trans*- and *cis*-corner sharing of the octahedra. The same type of sawtooth HTB layers occur in the walentaite-group minerals (Grey *et al.*, 2020).

From the perspective of HTB layer octahedral tilting, the zirconolite 2*M* and 3*T* polytypes have the $P6_3/mmc$ type of tilt system (symmetrical 'breathing', Fig. 2b) with capping of the smaller triangles of Xa anions by $A'X_7$ mono-capped trigonal antiprisms as shown in Fig. 9. Unlike the pyrochlores where the capping polyhedron links to the small triangles of anions in the HTB layers both above and below, the $A'X_7$ polyhedron in zirconolites has only one flat triangular face and so has only one-sided capping. Alternate $A'X_7$ polyhedra along the chains cap the layers alternately above and below the polyhedra.

For zirconolite-2*M* the triangular base of the ZrO_7 polyhedron has O–O = 2.97 Å, and the O–O edge of an undistorted TiO_6 octahedron from BVS calculations is 2.77 Å. Substituting these values in equation 1 gives an octahedral tilt angle of 12.8°. This is considerably smaller than for cubic pyrochlore, reflecting the larger size of the capping cation relative to the B cation. The tilt angle measured from the crystal structure is 10.5° based on the movement of the apical anions and 17° based on the displacement of the equatorial anions. The disparity between the two values reflects the large angular distortions of the TiO_6 polyhedra, with O–Ti–O angles in the range 78.4 to 98.4° and O–O distances from 2.48 to 2.97 Å. The shortest O–O distances correspond to edges that are shared with trigonal bipyramidal TiO_5 polyhedra in the hexagonal rings. The in-plane Ti–O–Ti and out-of-plane Ti–O–Zr angles have almost the same ranges, 133.1 to 138.3 and 131.9 to 136.7°, respectively. This contrasts with the rhombohedral pyrochlore, $Mn_2La_3Sb_3O_{14}$, which has a similar tilt angle but has quite different in-plane Sb–O–Sb and out-of-plane Sb–O–Mn angles of 128.7 and 147.6, respectively, (Table 1). The geometry of the octahedral tilting in the zirconolite-3*T* polytype (Grey *et al.*, 2003) is almost identical to that reported above for the 2*M* polytype.

Alunite-supergroup minerals and related compounds

Alunite-supergroup minerals have the general formula $AB_3(TX_4)_2X'_6$ with wide ranges of large A cations, small B cations and with tetrahedral groups being mainly SO_4, PO_4, AsO_4 and X' = O, OH, F and H_2O (Bayliss *et al.*, 2010). Jarosite minerals, $AFe_3^{3+}(SO^4)_2(OH)_6$ are the most well-known of the alunite-supergroup minerals due to their role in acid mine drainage and metallurgical processes, their identification on Mars and their magnetic properties (Majzlan *et al.*, 2010; Mills *et al.*, 2013).).

The minerals have rhombohedral symmetry, $R\bar{3}m$, with a ≈ 7 Å, c ≈ 17 Å and with atoms at the following Wyckoff sites: *A* site = 3*a*: 0,0,0; *B* site = 9*d*: ½, 0, ½; *T* site = 6*c*: 0,0,*z*; *z* ≈ 0.3; *X*1 = 6*c*: *z* ≈ 0.4; *X*2 = 18*h*: *x*,–*x*, *z*: *x* ≈ 0.22, *z*≈ –0.05; and *X*3 = 18*h*: *x* ≈ ⅛, *z* ≈ 0.13.

The structure can be described as based on HTB layers with strongly tilted octahedra giving small and large triangular groupings of apical anions as shown in Fig. 2b. The small triangles are capped by TX_4 tetrahedra and the large triangles are capped by AX_6 flattened trigonal antiprisms. The complete coordination for A comprises two interpenetrating trigonal antiprisms; A co-ordinates to 6 Xe anions (site *X*3) in the form of an elongated prism and to 6 Xa anions (site *X*2) forming a flattened prism. Goreaud and Raveau (1980) have previously described the relationship of the alunite structure to that of pyrochlore with BX_6 sandwiched between opposing small triangles in the HTB layers in pyrochlore and AX_6 (the flattened trigonal prism) sandwiched between opposing large triangles in alunite (Fig. 10). In Table 2, are listed the results of octahedral tilting calculations for alunite supergroup members that cover a wide range of size differentials between the B cation and the capping T and A cations.

The jarosite minerals have the largest size disparity between B and T ($B = Fe^{3+}$, T = S) and the largest calculated tilt angle of 22°. They also appear to be the least strained of the alunite minerals. The deviation of the O–Fe–O angles from 90° is of the order of only 1° and the octahedral tilt angles measured from the displacements of the Xa and Xe anions vary by ~2°. The changing of the A cation size has no significant effect on the tilting but there is a

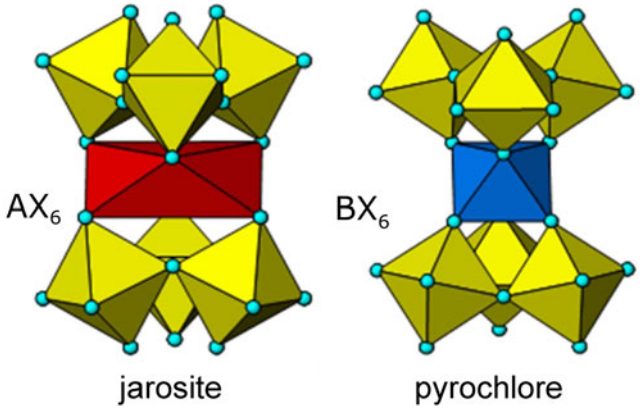

Fig. 10. Capping of large HTB triangles with AX_6 flattened trigonal antiprism in jarosite, compared with capping of small HTB triangles with BX_6 octahedron in pyrochlore (after Goreaud and Raveau, 1980).

https://doi.org/10.1180/mgm.2020.72 Published online by Cambridge University Press

Table 2. Structural data for alunite-supergroup minerals.

Mineral	Formula	Cell parameters (Å)		Φ calc. (°)	Φ from Xe, Xa, av. (°)	B–X–B (°)	A–Xe, A–Xa (Å)	Ref.
		a	*b*					
Alunite group								
Jarosite	$KFe_3(SO_4)_2(OH)_6$	7.291	17.144	22.0	22.5, 20.2 <21.3>	134.2	2.828, 2.964	[1]
Hydroniumjarosite	$(H_3O)Fe_3(SO_4)_2(OH)_6$	7.356	17.019	"	22.4, 20.9 <21.7>	134.4	2.811, 3.022	[2]
Natrojarosite	$NaFe_3(SO_4)_2(OH)_6$	7.327	16.732	"	23.2, 20.6 <21.9>	134.2	2.749, 2.966	[3]
Plumbogummite group								
Gorceixite	$BaAl_3((PO_{3.5}(OH)_{0.5})_2(OH)_6$	7.054	17.275	18.5	20.7, 17.7 <19.2>	136.0	2.859, 2.824	[4]
Goyazite	$SrAl_3((PO_{3.5}(OH)_{0.5})_2(OH)_6$	7.015	16.558	"	21.5, 17.6 <19.6>	136.4	2.729, 2.767	[5]
Crandallite	$CaAl_3((PO_{3.5}(OH)_{0.5})_2(OH)_6$	7.005	16.192	"	22.4, 18.5 <19.9>	136.1	2.670, 2.743	[6]
Dussertite group								
Arsenogoyazite	$SrAl_3((As,S)O_4)_2(OH)_6$	7.116	16.985	16.0	18.7, 14.3 <16.5>	139.2	2.836, 2.709	[7]
Philipsbornite	$Pb^{2+}Al_3((As,S)O_4)_2(OH)_6$	7.114	17.097	"	19.5, 15.1 <17.3>	138.4	2.852, 2.744	[8]
Arsenoflorencite-(La)	$LaAl_3(AsO_4)_2(OH)_6$	7.032	16.515	"	21.6, 14.1 <17.9>	137.4	2.653, 2.712	[9]

References: [1] Mills *et al.* (2013); [2] Majzlan *et al.* (2004); [3] Najorka *et al.* (2016); [4] Dzikowski *et al.* (2006); [5] Kato (1987); [6] Blount (1974); [7] U. Kolitsch (pers. comm.); [8] Cooper and Hawthorne (2012); and [9] Mills *et al.* (2010).

correlation between the A–Xe distance in the elongated trigonal prism and the cell parameter *c*. A linear correlation between the average ionic radius of the A cation and the *c* axis length has been reported for alunite-supergroup minerals by Sato *et al.* (2009). Because the TX_4 tetrahedra only cap the HTB layer on one side they cannot influence the interlayer spacing in the same way that the BX_6 double-capping octahedra can in pyrochlore structures. Instead the interlayer spacing in alunite-supergroup minerals is responsive to change in size of the A cation.

The plumbogummite group of minerals, gorceixite, goyazite and crandallite have a smaller Al^{3+} cation at the *B* site and a larger P^{5+} as a capping cation and the calculated tilt angle is correspondingly lowered to 18.5°. These minerals are more strained than the jarosites. The departure of the O–Al–O angles from 90° increases with decreasing A cation size from ± 2° for gorceixite to ± 3° for crandallite. In the latter mineral, the Ca cation is displaced from the 2*a* site to the more general 18*f* site (*x*,0,0, *x* = 0.044; Blount 1974) to meet its bonding and valence requirements. The strain is also manifested in a larger disparity (3 to 4°) between the octahedral tilt angles measured from the Xa and Xe displacements. At the smaller tilting angle relative to the jarosites, the large triangle of Xa anions is not as expanded as in jarosites and the A–Xa and A–Xe distances are closer to one another, with the ratio (A–Xa)/(A–Xe) even reversing from greater than 1 to less than 1 in the case of gorceixite.

The dussertite-group minerals have As^{5+} as the capping cation, larger than P^{5+} in the plumbogummite-group minerals and the tilting angle is correspondingly smaller at 16.0°. The AlO_6 polyhedra are even more distorted trigonal antiprisms than for the plumbogummite minerals, with O–Al–O angles in the range 85.0 to 95.0 for arsenoflorencite-(La) and greater discrepancies between the measured tilting angles. In the examples in Table 2, the A cations change from large monovalent cations in jarosites to smaller divalent cations in plumbogummites to even smaller trivalent and divalent cations in the dussertite-group minerals, with the added complication of Pb^{2+} having a lone pair electron configuration and a displacement from the 2*a* site to an 18*f* site as for crandallite. The observed increasing distortion of the Al-centred trigonal antiprisms must be a direct consequence of the A cation bonding and valence requirements having a more dominant role in establishing the equilibrium atomic arrangement.

The compound $NH_4(V^{5+}O_2)_3(Se^{4+}O_3)_2$ (Vaughey *et al.*, 1994) is closely related to alunite-supergroup minerals, as is evident when its formula is written as $NH_4V_3(SeO_3)_2O_6$. In this compound, HTB layers of VO_6 octahedra are capped by SeO_3 trigonal pyramids. The compound has hexagonal symmetry, space group $P6_3$, with *a* = 7.137 Å and *c* = 11.462 Å. In contrast to alunite minerals, where the tetrahedral apices point to the centres of hexagonal rings in adjacent HTB layers, the selenite compound has two independent SeO_3 groups with the pyramids on one side of each HTB layer pointing towards the hexagonal ring in the adjacent layer and the SeO_3 on the opposite side of each HTB layer pointing towards the larger triangle of Xa anions in the adjacent layer. This arrangement has a 2-layer hexagonal repeat compared to the 3-layer rhombohedral repeat for alunite minerals. The base of the SeO_3 pyramids and the average edge distance for the AlO_6 octahedra are almost identical so the tilting angle is almost the same as in pyrochlore structures, 15.5 Å. The polar compounds $A_2(WO_3)_3SeO_3$ (A = NH_4, Rb and Cs; Harrison *et al.*, 1995) and $A_2(MoO_3)_3SeO_3$ (A = Rb and Tl; Chang *et al.*, 2010) are also related closely to the alunite structure. In these compounds, with space group $P6_3$ and similar cell dimensions to the above compound, the SeO_3 trigonal pyramids cap the smaller triangles of the HTB layers on only one side of the layers. The compound $Cs_3Sb_3Ge_2O_{13}$ (Pagnoux *et al.*, 1993), space group $P6_3/mmc$, *a* = 7.31 Å and *c* = 16.73 Å, has an alunite-related structure based on HTB layers of SbO_6 octahedra, capped with GeO_4 tetrahedra. In this structure the GeO_4 tetrahedra in adjacent layers share their apical anion giving Ge_2O_7 groups that link the HTB layer together. The base of the GeO_4 tetrahedron is somewhat larger than the SbO_6 edge length and the calculated octahedral tilting angle is 14.2°, smaller than for the selenites.

The alunite-type structure is amenable to intergrowth with other structure types. In the perhamite-group minerals, perhamite and krasnoite (Mills *et al.*, 2006, 2012) pairs of alunite-type layers are intergrown with zeolitic groupings of cyclic Si_3O_9 linked into 4-member rings by corner sharing with AlO_4 tetrahedra. The latter corner-connect to the apical anions of the PO_4 tetrahedra of the alunite layers as shown in Fig. 11. The minerals are trigonal, $P\bar{3}m1$, with a ≈ 7.0 Å and c ≈ 20.2 Å. Perhamite has the composition $Ca_3Al_8Si_3P_4O_{24}(OH)_{14}{\cdot}8H_2O$. The intergrowth can be written as $2[Al_3X_{12}P_2XX_{½}] + [Al_2X_{2/2}Si_3X_9]$, where X = O or OH. Ca^{2+} cations and H_2O are located within 8-sided [100] channels located between the two intergrowth components as shown in Mills *et al.* (2006). The alunite-type layers have the composition of plumbogummite-group minerals and the calculated

https://doi.org/10.1180/mgm.2020.72 Published online by Cambridge University Press

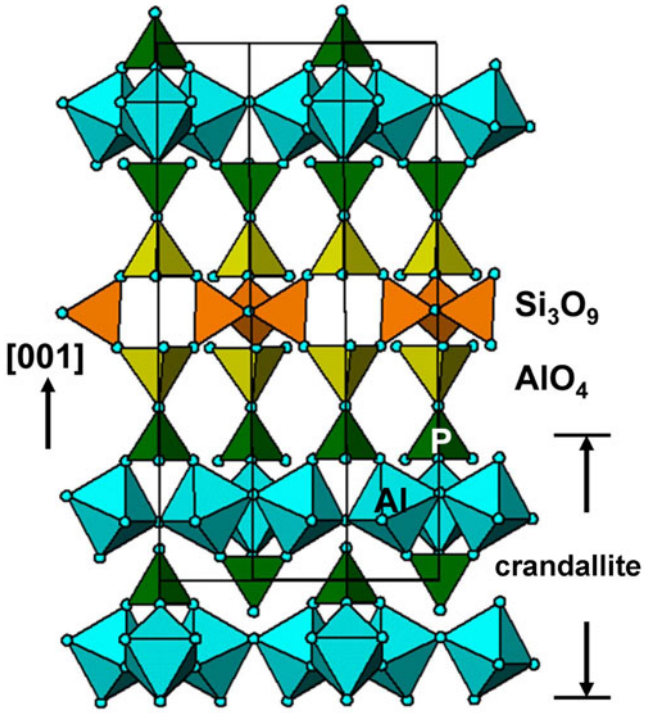

Fig. 11. Intergrowth of crandallite-type layers and zeolitic clusters in perhamite.

octahedral tilting is 18.5° (Table 2). The mineral iangreyite, $Ca_2Al_7(PO_4)_2(PO_3OH)_2(OH,F)_{15}{\cdot}8H_2O$ with space group *P*321, a ≈ 7.00 Å and c ≈ 16.7 Å, has a closely related intergrowth structure, in which the zeolitic $Al_2X_{2/2}Si_3X_9$ groups are replaced by AlX_5 trigonal bipyramids that share their apices with the PO_4 tetrahedra of the alunite-type layers (Mills *et al.*, 2011).

Weberite minerals and related compounds

Weberite is the name originally given to a fluoride mineral found in southern Greenland, with composition Na_2MgAlF_7 (Bøgvard, 1938). Its crystal structure was determined approximately by

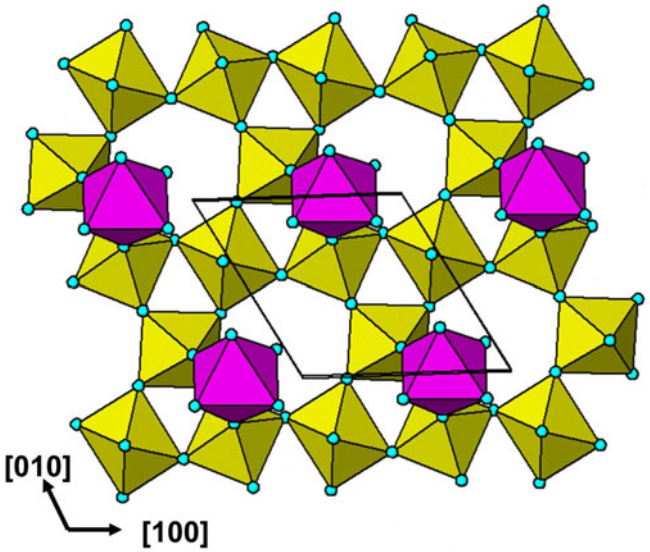

Fig. 12. Capping of HTB layer in weberite (polytype 3*T*).

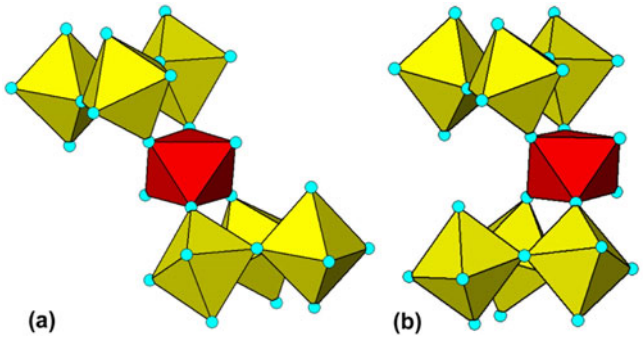

Fig. 13. Connectivity of capping octahedron to adjacent HTB layers in weberite. (*a*) *trans*-configuration; (*b*) *cis*-configuration.

Byström (1944) and refined by Giuseppetti and Tadini (1978) in space group *Imma*, with *a* = 7.060 Å, *b* = 10.000 Å and *c* = 7.303 Å. Like pyrochlore and zirconolite, weberite can be described as an ordered anion-deficient fluorite structure with general formula $A_2B_2X_7$ in which alternate $(111)_{fluorite}$ planes of composition AB_3 and A_3B form a *fcc* array (Cai and Nino, 2009; Grey *et al.*, 2003). The A_3 and B_3 arrays are both kagomé nets, parallel to (011) of the aristotype weberite cell with octahedral coordination of the small B cations to form a HTB network and 8-coordination of the large A cations. The weberite and pyrochlore structures differ in the location of the capping B cation in the A_3B layers. In pyrochlore the capping cation connects to eclipsed triangular arrays of Xa anions in the HTB layers on either side of the capping cation, whereas in weberite the capping cation coordinates to only two Xa anions on either side and completes its six-fold coordination with two unshared anions. As a result, the weberite small-cation framework has the composition B_2X_7 whereas the pyrochlore small-cation framework composition is B_2X_6.

The octahedra in the HTB layers of weberite undergo a different tilting scheme to that in pyrochlore. The octahedral tilting in weberite corresponds to the *Cmcm* space group type tilting reported by Campbell *et al.* (2018) and shown in Fig. 2c. In contrast to $P6_3/mmc$ tilting, where the triangular groupings of Xa anions all move in towards a central point or all move out, the *Cmcm* tilting results in pairs of Xe anions in one triangle moving inwards and the third anion moving out, with the reverse occurring in the adjacent triangle, thus producing pairs of compressed and elongated isosceles triangles. The pair of Xa anions that moves in as a result of tilting provides the base for connection

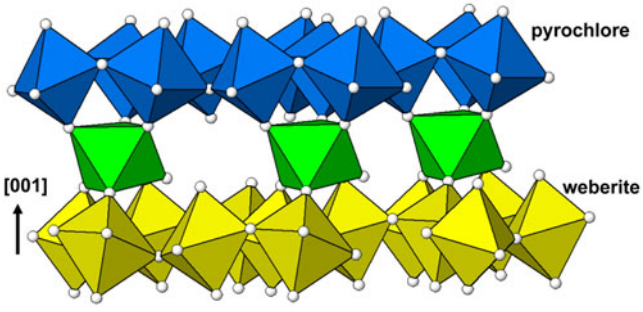

Fig. 14. Interface layer of capping octahedra between pyrochlore-type and weberite-type layers in $(Ca,Sm)_2Ta_2O_7$-5*M*.

https://doi.org/10.1180/mgm.2020.72 Published online by Cambridge University Press

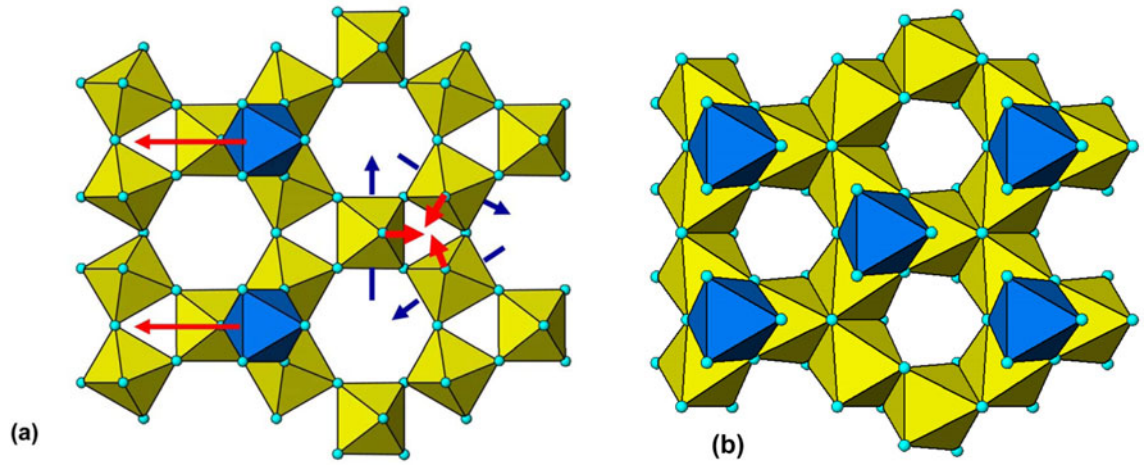

Fig. 15. (*a*) Tilting of octahedra in HTB layer by 54.7°, with displacement of capping octahedron and loss of apical anions to give (*b*) spinel-type structure.

of the capping cation in weberite. The HTB layer and its capping octahedra are shown in Fig. 12.

There are three different ways that a second HTB layer can join to two Xa anions of the capping octahedra in Fig. 13. One of the connections results in the unshared anions being in a *trans* configuration, shown in Fig. 13a while the other two connections have the unshared anions in a *cis* configuration, shown in Fig. 13b. The different sequences of capping configurations lead to several different weberite polytypes, distinguished by symmetry and the number of HTB layers. The aristotype mineral is weberite 2*O* (2-layer orthorhombic) and it has the unshared anions of the capping octahedra in *trans* configuration. Other weberite polytypes include 2*M*, 4*M*, 5*M*, 6*M*, 7*M*, 3*T*, 6*T* and 8*O* (Cai and Nino, 2009). In all polytypes except the arisotype 2O, the unit cells have a hexagonal (a ≈ 7.3 Å) or orthohexagonal base and a repeat normal to the base of $n \times 6$ Å, where 6 Å is the interlayer separation for the (001) HTB layers.

The weberite 2*M* polytpe with space group C2/c and cell parameters $a \approx 12.3$ Å, $b \approx 7.3$ Å, $c \approx 12.8$ Å and $\beta \approx 109.3°$ has the capping octahedra in *cis* configuration whereas the 4*M* polytype with doubled *c* axis has an alternation of *cis* and *trans* configurations. Similarly the 3*T* polytype, with space group $P3_121$, $a \approx 7.3$ Å and $c \approx 18$ Å has each of the three capping octahedra in *cis* configuration while the 6*T* polytype with space group $P3_1$ and doubled *c* axis has an alternation of *cis* and *trans* octahedra.

Doped $Ca_2Ta_2O_7$ compounds have been structurally characterised as 5*M*, 6*M* and 7*M* polytypes (Grey *et al.*, 1999, 2001, Grey and Roth, 2000). These compounds differ from other weberite polytypes in having periodic pseudo-unit-cell twinning of the cation layers ("pseudo" because B is reflected into A across the twin plane). The twin planes are on B_3A layers and correspond to elements of hexagonal stacking of the layers. For example, the 6*M* polytype has a stacking sequence *hccccchcccch*. In the *h*-stacked layers the kagomé net is corrugated, with cations displaced along [001] by ± 0.15 Å. The 5-layer cubic-stacked blocks correspond to weberite type. The 5*M* polytype exists in two structural forms, which have the same unit cell and space group, *C*2, and the same layer stacking sequence of *hcchcccccch*, but Nb-doped 5*M* $Ca_2Ta_2O_7$ has weberite blocks between the *h*-stacked layers and Sm-doped 5*M* $Ca_2Ta_2O_7$ has weberite in the 5-layer-wide *fcc* block and pyrochlore in the 3-layer-wide block. The interface capping layer and adjacent HTB layers in this structure is shown in Fig. 14. The octahedral tilting changes from $P6_3/mmc$-type in the pyrochlore blocks to *Cmcm*-type in the weberite blocks, so that the capping octahedra shown in Fig. 14 share 3 anions with octahedra in the pyrochlore $CaTa_3$ layer on one side and only two anions with octahedra in the weberite $CaTa_3$ layer on the opposite side.

Octahedral tilting by $\sin^{-1}(\sqrt{2}/\sqrt{3})$; transformation of HTB corner sharing to edge sharing

Substitution of $\Phi = \sin^{-1}(\sqrt{2}/\sqrt{3}) = 54.73°$ (half the tetrahedral angle) into equation 1 gives Xa–Xa = 0. i.e. the three Xa anions meet at a point. This octahedral tilting angle results in the triangles of corner-shared octahedra in the HTB layer being converted to triangles of edge-shared octahedra, with loss of four anions per triangle. Formally, for a trivalent metal hydrated HTB layer the transformation can be written as a dehydration: $M_3^{3+}(OH)_9(H_2O)_3 \rightarrow M_3^{3+}O(OH)_7 + 4H_2O$. The hexagonal kagomé net is maintained but it has shrunk from $(1 + \sqrt{3})e$ to $2e$ where *e* is the octahedral edge.

In Fig. 15 is shown the case where the triangles of Xa anions are capped by octahedra as in pyrochlore. Tilting of the octahedra and displacement of the capping cations to the adjacent triangles as shown in the Figure converts the pyrochlore network, M_4X_{12}, to the spinel network of edge-shared octahedra, M_4X_8 with loss of 4X. The octahedral framework in spinel has the same 3D kagomé net of corner-connected B_4 tetrahedra as in pyrochlore. Another family of minerals with the same topology is the paratacamite group, of which an example is herbertsmithite, $Cu_3Zn(OH)_6Cl_2$ (Malcherek *et al.*, 2018). In herbertsmithite Cu^{2+} cations form the kagomé net and Zn^{2+} are the capping cations.

Acknowledgments. The author thanks Dr. Chris Howard for advice on different octahedral tilt systems in hexagonal tungsten bronze compounds, Dr. Patrick Woodward for advice on the driving forces for octahedral tilting in perovskites and two reviewers for helpful comments.

References

Andrade M.B., Atencio D., Chukanov N.V. and Ellena J. (2013) Hydrokenomicrolite, $(\square,H_2O)_2Ta_2(O,OH)_6(H_2O)$, a new microlite-group mineral from Volta Grande pegmatite, Nazareno, Minas Gerais, Brazil. *American Mineralogist*, **98**, 292–296.

Atencio D., Andrade M.B., Christy A.G., Gieré R. and Kartashov P.M. (2010) The pyrochlore supergroup of minerals: nomenclature. *The Canadian Mineralogist*, **48**, 673–698.

https://doi.org/10.1180/mgm.2020.72 Published online by Cambridge University Press

Atencio D., Ciriotti M.E. and Andrade M.B. (2013) Fluorcalcioroméite, (Ca, $Na)_2Sb_2^{5+}(O,OH)_6F$, a new roméite-group mineral from Starlera mine, Ferrera, Grischun, Switzerland: description and crystal structure. *Mineralogical Magazine*, **77**, 467–473.

Atencio D., Andrade M.B., Bastos Neto A.C. and Pereira V.P. (2017) Ralstonite renamed hydrokenoralstonite, coulsellite renamed fluornatrocoulsellite, and their incorporation into the pyrochlore supergroup. *The Canadian Mineralogist*, **55**, 115–120.

Bayliss P., Mazzi F., Munno R. and White T.J. (1989) Mineral nomenclature: zirconolite. *Mineralogical Magazine*, **53**, 565–569.

Bayliss P., Kolitsch U., Nickel E.H. and Pring A. (2010) Alunite supergroup: recommended nomenclature. *Mineralogical Magazine*, **74**, 919–927.

Biagioni C., Orlandi P., Nestola F. and Bianchin S. (2013) Oxycalcioroméite, $Ca_2Sb_2O_6O$, from Buca della Vena mine, Apuan Alps, Tuscany, Italy: a new member of the pyrochlore supergroup. *Mineralogical Magazine*, **77**, 3027–3037.

Birch W.D., Pring A., Reller A. and Schmalle H. (1992) Bernalite: a new ferric hydroxide with perovskite structure. *Naturwissenschaften*, **79**, 509–511.

Birch W.D., Grey I.E., Mills S.J., Bougerol C., Pring A. and Ansermet S. (2007) Pittongite, a new tungstate with a mixed-layer, pyrochlore-hexagonal tungsten bronze structure, from Victoria, Australia. *The Canadian Mineralogist*, **45**, 857–864.

Blount A.M. (1974) The crystal structure of crandallite. *American Mineralogist*, **59**, 41–47.

Bøgvard R. (1938) Weberite, a new mineral from Ivigtut, *Meddelelser om Grønland*, **119**, 1–11.

Bonazzi P., Bindi L., Zoppi M., Capitani G.C. and Olmi F. (2006) Single-crystal diffraction and transmission electron microscopy studies of "silicified" pyrochlore from Narssâssuk, Julianehaab district, Greenland. *American Mineralogist*, **91**, 794–801.

Brese N.E. and O'Keeffe M. (1991) Bond-valence parameters for solids. *Acta Crystallographica*, **B47**, 192–197.

Byström A. (1944) The structure of weberite, Na_2MgAlF_7. *Arkiv foer Kemi, Mineralogi och Geologi*, **18B**, 1–7.

Cai L. and Nino J.C. (2009) Complex ceramic structures. I Weberites. *Acta Crystallographica*, **B65**, 269–290.

Campbell B., Howard C.J., Averett T.B., Whittle T.A., Schmid S., Yost C. and Stokes H.T. (2018) An algebraic approach to cooperative rotations in networks of interconnected rigid units. *Acta Crystallographica*, **A74**, 408–424.

Chang H.Y., Kim S.W. and Halasyamani P.S. (2010) Polar hexagonal tungsten oxide (HTO) materials: (1) Synthesis, characterization, functional properties, and structure – property relationships in $A_2(MoO_3)_3(SeO_3)$ ($A = Rb^+$ and Tl^+) and (2) Classification, structural distortions, and second-harmonic generating properties of known polar HTOs. *Chemistry of Materials*, **22**, 3241–3250.

Christy A.G. and Atencio D. (2013) Clarification of status of species in the pyrochlore supergroup. *Mineralogical Magazine*, **77**, 13–20.

Chukanov N.V., Zubkova N.V., Pekov I.V., Vigasina M.F., Polekhovsky Y.S., Ternes B., Schüller W., Britvin S.N. and Pushcharovsky D.Yu. (2019) Stefanweissite, $(Ca,REE)_2Zr_2(Nb,Ti)(Ti,Nb)_2Fe^{2+}O_{14}$, a new zirconolite-related mineral from the Eifel paleovolcanic region, Germany. *Mineralogical Magazine*, **83**, 607–614.

Cooper M.A. and Hawthorne F.C. (2012) Refinement of the crystal structure of zoned philipsbornite-hidalgoite from the Tsumeb mine, Namibia, and hydrogen bonding in the $D^{2+}G_3^{3+}(T^{5+}O_4)(TO_3OH)(OH)_6$ alunite structures. *Mineralogical Magazine*, **76**, 839–849.

Courbion G., Jacoboni C. and De Pape R. (1976) La structure crystalline de $Cs_2NaAl_3F_{12}$. *Acta Crystallographica*, **B32**, 3190–3193.

Crosnier M.P., Pagnoux C., Guyomard D., Verbaere A., Piffard Y. and Tournoux M. (1991) The crystal structure of a novel cyclotrisilicate: $Cs_8Nb_{10}O_{23}\square(Si_3O_9)_2$, Its relationship with the pyrochlore and benitoite types. *European Journal of Solid State Inorganic Chemistry*, **28**, 971–981.

Dzikowski T., Groat L.A. and Jambor J.L. (2006) The symmetry and crystal structure of gorceixite, $BaAl_3[PO_3(O,OH)]_2(OH)_6$, a member of the alunite supergroup. *The Canadian Mineralogist*, **44**, 951–958.

Fu W.T. and Ijdo D.J.W. (2014) Crystal structure of $Mn_2Ln_3Sb_3O_{14}$ (Ln = La, Pr and Nd): a new ordered rhombohedral pyrochlore. *Journal of Solid State Chemistry*, **213**, 165–168.

Fuentes A.F., Montemayor S.M., Maczka M., Lang M., Ewing R.C. and Amador U. (2018) A critical review of existing criteria for the prediction of pyrochlore formation and stability. *Inorganic Chemistry*, **57**, 12093–12105.

Gagné O.C. and Hawthorne F.C. (2015) Comprehensive derivation of bond-valency parameters for ion pairs involving oxygen. *Acta Crystallographica*, **B71**, 562–578.

Gatehouse B.M., Grey I.E., Hill R.J. and Rossell H.J. (1981) Zirconolite, $CaZr_xTi_{3-x}O_7$; structure refinements for near-end-member compositions with $x = 0.85$ and 1.30. *Acta Crystallographica*, **B37**, 306–312.

Gerand B., Nowogrocki G. and Figlarz M. (1981) A new tungsten trioxide hydrate, $WO_3{\cdot}⅓H_2O$: Preparation, characterization and crystallographic study. *Journal of Solid State Chemistry*, **38**, 312–320.

Giuseppetti G. and Tadini C. (1978) Re-examination of the crystal structure of weberite. *Tschermaks Mineralogische und Petrographische*, **25**, 57–62.

Grey I.E., Roth R.S., Mumme G., Bendersky L.A. and Minor D. (1999) Crystal chemistry of new calcium tantalate dielectric materials. *Materials Research Society Symposium Proceedings*, **547**, 127–138.

Grey I.E. and Roth R.S. (2000) New calcium tantalate polytypes in the system $Ca_2Ta_2O_7$–$Sm_2Ti_2O_7$. *Journal of Solid State Chemistry*, **150**, 167–177.

Grey I.E., Roth R.S., Mumme W.G., Planes J., Bendersky L., Li C. and Chenavas J. (2001) Characterization of new 5M and 7M polytypes of niobia-doped $Ca_2Ta_2O_7$. *Journal of Solid State Chemistry*, **161**, 274–287.

Grey I.E., Mumme W.G., Ness T.J., Roth R.S. and Smith K.L. (2003) Structural relations between weberite and zirconolite polytypes – refinements of doped 3T and 4M $Ca_2Ta_2O_7$ and 3T $CaZrTi_2O_7$. *Journal of Solid State Chemistry*, **174**, 285–295.

Grey I.E., Birch W.D., Bougerol C. and Mills S.J. (2006) Unit-cell intergrowth of pyrochlore and hexagonal tungsten bronze structures in secondary tungsten minerals. *Journal of Solid State Chemistry*, **179**, 3860–3869.

Grey I.E., Mumme W.G., Vanderah T.A., Roth R.S. and Bougerol C. (2007) Chemical twinning of the pyrochlore structure in the system Bi_2O_3–Fe_2O_3–Nb_2O_5. *Journal of Solid State Chemistry*, **180**, 158–166.

Grey I.E., Mumme W.G. and MacRae C.M. (2013) Lead-bearing phyllotungstite from the Clara mine, Germany with an ordered pyrochlore-hexagonal tungsten bronze intergrowth structure. *Mineralogical Magazine*, **77**, 57–67.

Grey I.E., Hochleitner R., Rewitzer C., Riboldi-Tunnicliffe A., Kampf A.R., MacRae C.M., Mumme W.G., Kaliwoda M., Friis H. and Martin C.U. (2020) The walentaite group and the description of a new member, alcantarillaite, from the Alcantarilla mine, Belalcazar, Cordoba, Andalusia, Spain. *Mineralogical Magazine*, **84**, 412–419.

Goreaud M. and Raveau B. (1980) Alunite and crandallite: a structure derived from that of pyrochlore. *American Mineralogist*, **65**, 953–956.

Groult D., Pannetier J. and Raveau B. (1982) Neutron diffraction study of defect pyrochlores $TaWO_{5.5}$, $HTaWO_6$, $H_2Ta_2O_6$ and $HTaWO_6{\cdot}H_2O$. *Journal of Solid State Chemistry*, **41**, 277–285.

Hålenius U. and Bosi F. (2013) Oxyplumboroméite, $Pb_2Sb_2O_7$, a new mineral species of the pyrochlore supergroup from Harstigen mine, Värmland, Sweden. *Mineralogical Magazine*, **77**, 2931–2939.

Harrison T.A., Dussack L.L., Vogt T. and Jacobson A.J. (1995) Syntheses, crystal structures, and properties of new layered tungsten(VI)-containing materials based on the hexagonal-WO_3 structure: $M_2(WO_3)_3SeO_3$ ($M = NH_4$, Rb, Cs). *Journal of Solid State Chemistry*, **120**, 112–120.

Hogarth D.D. (1977) Classification and nomenclature of the pyrochlore group. *American Mineralogist*, **62**, 403–410.

Ivanyuk G.Y., Yakovenchuk V.N., Panikorovskii T.L., Konoplyova N., Pakhomovsky Y.A., Bazai A.V., Bocharov V.N. and Krivovichev S.V. (2019) Hydroxynatropyrochlore, $(Na,Ca,Ce)_2Nb_2O_6(OH)$, a new member of the pyrochlore group from the Kovdor phoscorite–carbonatite pipe, Kola Peninsula, Russia. *Mineralogical Magazine*, **83**, 107–113.

Kasatkin A.V., Britvin S.N., Peretyazhko I.S., Chukanov N.V., Škoda R. and Agakhanov A.A. (2020) Oxybismutomicrolite, a new pyrochlore-supergroup mineral from the Malkan pegmatite field, central Transbaikalia, Russia. *Mineralogical Magazine*, **84**, 444–454.

Kato T. (1987) Further refinement of the goyazite structure. *Mineralogical Journal*, **13**, 390–396.

Krivovichev S.V. (2008). Minerals with antiperovskite structure: a review. *Zeitschrift für Kristallographie*, **223**, 109–113.

https://doi.org/10.1180/mgm.2020.72 Published online by Cambridge University Press

Kunz M. and Brown I.D. (1995) Out-of-center distortions around octahedrally coordinated d^0 transition metals. *Journal of Solid State Chemistry*, **115**, 395–406.

Labbé P., Goreaud M., Raveau B. and Monier J.C. (1978) Etude comparative des structures M_xWO_3 de type bronze hexagonal. I. Analyse structural des bronzes de composition $M_{0.30}WO_3$. Stéréochimie des elements M = Rb^1, Tl^1 et In^1. *Acta Crystallographica*, **B34**, 1433–1438.

Le Bail A. (2009) Thermodiffractometry and crystal structures of the hexagonal-tungsten-bronze-related $K_3Al_3F_{12}{\cdot}nH_2O$ (n = 2,1). *Powder Diffraction*, **24**, 292–300.

Le Bail A., Jacoboni C., Leblanc M., De Pape R., Duroy H. and Fourquet L. (1988) Crystal structure of the metastable form of aluminium trifluoride, β-AlF_3 and the gallium and indium homologs. *Journal of Solid State Chemistry*, **77**, 96–101.

Le Bail A., Gao Y., Fourquet J.L. and Jacobini C. (1990) Structure determination of $A_2NaAl_3F_{12}$ (A = K, Rb). *Materials Research Bulletin*, **25**, 831–839.

Leblanc M., Ferey G., Chevallier P., Calage Y. and De Pape R. (1983) Hexagonal tungsten bronze-type Fe^{III} fluoride: $(H_2O)_{0.33}FeF_3$; crystal structure, magnetic properties, dehydration to a new form of iron trifluoride. *Journal of Solid State Chemistry*, **47**, 53–58.

Li G. and Xue Y. (2018) Wumuite, IMA 2017-067a. CNMNC Newsletter No. 44, August 2018, page 1018; *Mineralogical Magazine*, **82**, 1015–1021.

Li G., Xue Y. and Xiong M. (2019) Tewite: a K-Te-W new mineral species with a modified tungsten-bronze type structure, from the Panzhihua-Xichang region, southwest China. *European Journal of Mineralogy*, **31**, 145–152.

Lumpkin G.R. and Ewing R.C. (1995) Geochemical alteration of pyrochlore group minerals: pyrochlore subgroup. *American Mineralogist*, **80**, 732–743.

Magneli A. (1952) Tungsten bronzes containing six-membered rings of WO_3 octahedra. *Nature*, **169**, 791–792.

Magneli A. (1953) Studies on the hexagonal tungsten bronzes of potassium, rubidium and cesium. *Acta Chemica Scandinavica*, **7**, 315–324.

Majzlan J., Stevens R., Boerio-Goates J., Woodfield B.F., Navrotsky A., Burns P.C., Crawford M.K. and Amos T.G. (2004) Thermodynamic properties, low-temperature heat-capacity anomalies, and single-crystal X-ray refinement of hydronium jarosite, $(H_3O)Fe_3(SO_4)_2(OH)_6$. *Physics and Chemistry of Minerals*, **31**, 518–531.

Majzlan J., Glasnak P., Fisher R.A., White M.A., Johnson M.B., Woodfield B. and Boerio-Goates J. (2010) Heat capacity, entropy, and magnetic properties of jarosite-group compounds. *Physics and Chemistry of Minerals*, **37**, 635–651.

Malcherek T., Welch M.D. and Williams P.A. (2018) The atacamite family of minerals – a testbed for quantum spin liquids. *Acta Crystallographica*, **B74**, 519–526.

Matsubara S., Kato A., Shimizu M., Sekiuchi K. and Suzuki Y. (1996) Romeite from the Gozaisho mine, Iwaki, Japan. *Mineralogical Journal*, **18**, 155–160.

McNulty J.A., Gibbs A.S., Lightfoot P. and Morrison F.D. (2019) Octahedral tilting in the polar tungsten bronzes $RbNbW_2O_9$ and $KNbW_2O_9$. *Acta Crystallographica*, **B75**, 815–821.

McQueen T.M., West D.V., Muegge B., Huang Q., Noble K., Zandbergen H.W. and Cava R.J. (2008) Frustrated ferroelectricity in niobate pyrochlores. *Journal of Physics: Condensed Matter*, **20**, 235210.

Mills S., Mumme G., Grey I. and Bordet P. (2006) The crystal structure of perhamite. *Mineralogical Magazine*, **70**, 201–209.

Mills S.J., Kartashov P.M., Kampf A.R. and Raudsepp M. (2010) Arsenoflorencite-(La), a new mineral from the Komi Republic, Russian Federation: description and crystal structure. *European Journal of Mineralogy*, **22**, 613–621.

Mills S.J., Kampf A.R., Sejkora J., Adams P.M., Birch W.D. and Plásil J. (2011) Iangreyite: a new secondary phosphate mineral closely related to perhamite. *Mineralogical Magazine*, **75**, 327–336.

Mills S.J., Sejkora J., Kampf A.R., Grey I.E., Bastow T.J., Ball N.A., Adams P.M., Raudsepp M. and Cooper M.A. (2012) Krásnoite, the fluorophosphate analogue of perhamite from the Huber open pit, Czech Republic and the Silver Coin mine, Nevada, USA. *Mineralogical Magazine*, **76**, 625–634.

Mills S.J., Nestola F., Kahlenberg V., Christy A.G., Hejny C. and Redhammer G.J. (2013) Looking for jarosite on Mars: The low-temperature crystal structure of jarosite. *American Mineralogist*, **98**, 1966–1971.

Mills S.J., Christy A.G., Rumsey M.S. and Spratt J. (2016) The crystal chemistry of elsmoreite from the Hemerdon (Drakelands) mine, UK: hydrokenoelsmoreite-3*C* and hydrokenoelsmoreite-6*R*. *Mineralogical Magazine*, **80**, 1195–1203.

Mizoguchi H., Woodward P.M., Byeon S-H. and Parise J.B. (2004). Polymorphism in $NaSbO_3$: structure and bonding in metal oxides. *Journal of the American Chemical Society*, **126**, 3175–3184.

Mumme W.G., Grey I.E., Birch W.D., Pring A., Bougerol C. and Wilson N.C. (2010) Coulsellite, $CaNa_3AlMg_3F_{14}$, a rhombohedral pyrochlore with 1:3 ordering in both A and B sites, from the Cleveland mine, Tasmania, Australia. *American Mineralogist*, **95**, 736–740.

Najorka J., Lewis J.M., Spratt J. and Sephton M.A. (2016) Single-crystal X-ray diffraction study of synthetic sodium-hydronium jarosite. *Physics and Chemistry of Minerals*, **43**, 377–386.

O'Keeffe M. and Hyde B.G. (1980) Plane nets in crystal chemistry. *Philosophical Transactions of the Royal Society of London*, **A295**, 553–623.

Pagnoux C., Verbaere A., Piffard Y. and Tournoux M. (1993) Crystal structure of $Cs_3Sb_3O_6(Ge_2O_7)$, its relationship with $K_3Sb_3O_6(PO_4)_2$. *European Journal of Solid State and Inorganic Chemistry*, **30**, 111–123.

Pannetier J. and Lucas J. (1970) Nouvelle description de la structure pyrochlore de compose $Cd_2Nb_2O_6S$. *Materials Research Bulletin*, **5**, 797–806.

Pati S.K. and Rao C.N.R. (2008) Kagome network compounds and their novel magnetic properties. *Chemical Communications*, **2008**, 4683–4693.

Prinz H. (1992) Ein neues Syntheseverfahren für die Wolframbronze $Cs_{0.29}WO_3$ und ihre Kristallstruktur. *Zeitschrift für Anorganische und Allgemische Chemie*, **609**, 95–98.

Pye M.F. and Dickens P.G. (1979) A structural study of the hexagonal tungsten bronze, $K_{0.26}WO_3$. *Materials Research Bulletin*, **14**, 1397–1402.

Sato E., Nakai I., Miyawaki R. and Matsubara S. (2009) Crystal structures of alunite family minerals: beaverite, corkite, alunite, natroalunite, jarosite, svanbergite, and woodhouseite. *Neues Jahrbuch für Mineralogie, Abhandlungen*, **185**, 313–322.

Subramanian M.A., Aravamudan G. and Subba Rao G.V. (1983) Oxide pyrochlores – a review. *Progress in Solid State Chemistry*, **15**, 55–143.

Syôzi I. (1951) Statistics of kagomé lattice. *Progress of Theoretical Physics*, **VI**, 306–308.

Tarassov M.P. and Tarassova E.D. (2018) Structural and chemical evolution of mineral forms of tungsten in the oxidation zone of the Grantcharitza deposit (Western Rhodopes, Bulgaria). *Bulgarian Chemical Communications*, **50**, 270–280.

Trump B.A., Koohpayeh S.M., Livi K.J.T., Wen J.-J., Arpoino K.E., Ramasse Q.M., Brydson R., Feygenson M., Takeda H., Takigawa M., Kimura K., Nakatsuji S., Broholm C.L. and McQueen T.M. (2018) Universal geometric frustration in pyrochlores. *Nature Communications*, **2018**, 1–10.

Vaughey J.T., Harrison T.A., Dussack L.L. and Jacobson A.J. (1994) A new layered vanadium selenium oxide with a structure related to hexagonal tungsten oxide: $NH_4(VO_2)_3(SeO_3)_2$. *Inorganic Chemistry*, **33**, 4370–4375.

Walenta K. (1984) Phyllotungstit, ein neues sekondäres Wolframmineral aus der Grube Clara im mittleren Schwarzwald. *Neues Jahrbuch für Mineralogie-Monatshafte*, **1984**, 529–535.

Whittle T.A., Schmid S. and Howard C.H. (2015) Octahedral tilting in the tungsten bronzes. *Acta Crystallographica*, **B71**, 342–348.

Whittle T.A., Schmid S. and Howard C.J. (2018) Octahedral tilting in the tungsten bronzes. Addendum. *Acta Crystallographica*, **B74**, 742–744.

Witzke T., Steins M., Doering T., Schuckmann W., Wegner R. and Pollmann H. (2011) Fluornatromicrolite, $(Na,Ca,Bi)_2Ta_2O_6F$, A new mineral species from Quixaba, Paraiba, Brazil. *The Canadian Mineralogist*, **49**, 1105–1110.

Yin J., Li G., Yang G., Ge X., Xu H. and Wang J. (2015) Fluornatropyrochlore, a new pyrochlore supergroup mineral from the Boziguoer rare earth element deposit, Baicheng County, Akesu, Xinjiang, China. *The Canadian Mineralogist*, **53**, 455–460.

Zubkova N.V., Chukanov N.V., Pekov I.V., Ternes B., Schüller W. and Pushcharovsky D. Yu. (2018) The structure of nonmetamict Nb-rich zirconolite-3T from the Eifel paleovolcanic region, Germany. *Zeitschrift für Kristallographie*, **233**, 463–468.

https://doi.org/10.1180/mgm.2020.72 Published online by Cambridge University Press